

PSDNorm: Test-Time Temporal Normalization for Deep Learning on EEG Signals

Théo Gnassounou¹ Antoine Collas¹ Rémi Flamary² Alexandre Gramfort¹

Abstract

Distribution shift poses a significant challenge in machine learning, particularly in biomedical applications such as EEG signals collected across different subjects, institutions, and recording devices. While existing normalization layers, BatchNorm, LayerNorm and InstanceNorm, help address distribution shifts, they fail to capture the temporal dependencies inherent in temporal signals. In this paper, we propose PSDNorm, a layer that leverages Monge mapping and temporal context to normalize feature maps in deep learning models. Notably, the proposed method operates as a test-time domain adaptation technique, addressing distribution shifts without additional training. Evaluations on 10 sleep staging datasets using the U-Time model demonstrate that PSDNorm achieves state-of-the-art performance at test time on datasets not seen during training while being 4x more data-efficient than the best baseline. Additionally, PSDNorm provides a significant improvement in robustness, achieving markedly higher F1 scores for the 20% hardest subjects.

1. Introduction

Data Shift in Physiological Signals Machine learning techniques have achieved remarkable success in various domains, including computer vision, biology, audio processing, and language understanding. However, these methods face significant challenges when there are distribution shifts between training and evaluation datasets. For example, in biological data, such as electroencephalography (EEG) signals, the distribution of the data can vary significantly. Indeed, data is collected from different subjects, electrode positions, and recording conditions. This paper focuses on sleep staging, a task that consists of classifying the sleep stages of

a subject based on EEG signals during one night of sleep. Depending on the dataset, the cohort can be composed of different age groups, sex repartition, health conditions, and recording conditions. Such variability brings shift in the distribution making challenging the generalization of the model to unseen datasets.

Normalization to Address Data Shift Normalization layers are widely used in deep learning models to improve neural network training and generalization. The most commonly used normalization layers include BatchNorm (Ioffe & Szegedy, 2015), LayerNorm (Ba et al., 2016), and InstanceNorm (Ulyanov, 2016). BatchNorm computes statistics across the batch to normalize each feature, while LayerNorm normalizes all features within each individual sample. InstanceNorm applies normalization independently to each channel within a sample. Other normalization layers have been proposed for specific tasks such as (Kobler et al., 2022) for covariance matrices of EEG signals or (Kim et al., 2021) for time-series forecasting. However, these normalization layers have been shown to be insufficient to address data distribution shifts in the temporal correlation of signals. Hence, normalizations for sleep staging segmentation have been proposed as a pre-processing step either over an entire night of recordings (Apicella et al., 2023) or within smaller temporal windows (Chambon et al., 2018). However, recent studies (Gnassounou et al., 2023; 2024) show that taking into account temporal correlation is important when normalizing, and proposed the Temporal Monge Alignment (TMA) method, which aligns the Power Spectral Density (PSD) of signals to a common reference using Monge mapping.

Domain Generalization In sleep staging, numerous neural network architectures have been proposed to classify sleep stages. These models can process data in different formats, including raw signal inputs (Chambon et al., 2018; Perslev et al., 2021; Guillot & Thorey, 2021), spectrogram representations (Phan et al., 2023; 2019), or a combination of both (Phan et al., 2022). While many models are typically evaluated on a limited number of datasets, the work by (Perslev et al., 2021) introduced U-Sleep, a model trained on a large-scale dataset of sleep recordings. Their architecture, based on U-Time (Perslev et al., 2019), incorporates

¹Université Paris-Saclay, Inria, CEA, 91120 Palaiseau, France

²École Polytechnique, IP Paris, CMAP, UMR 7641, 91120 Palaiseau, France. Correspondence to: Théo Gnassounou <theo.gnassounou@inria.fr>.

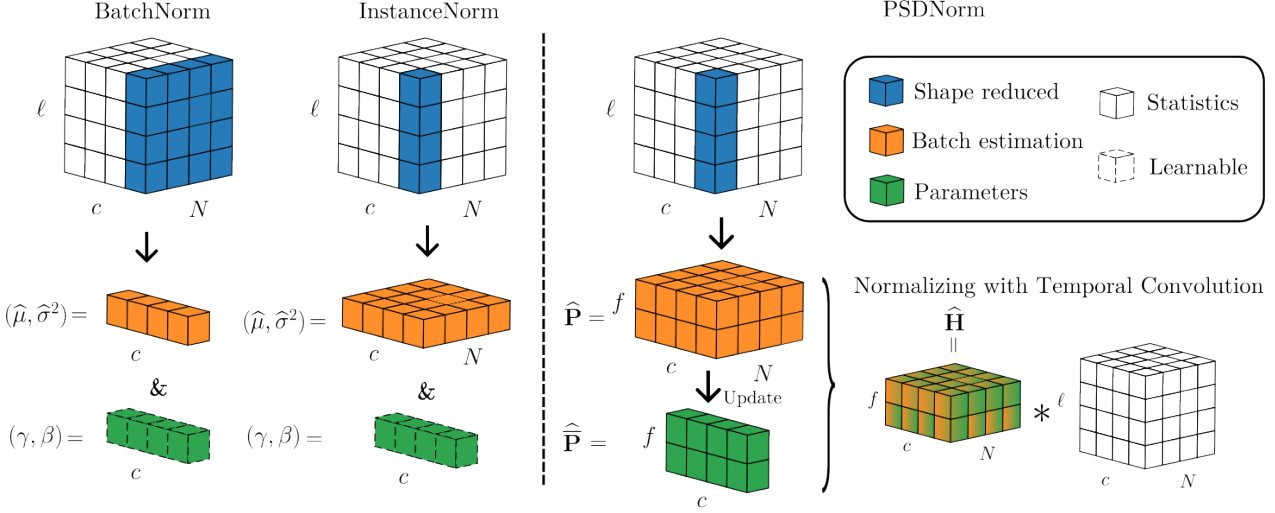


Figure 1: **Description of normalization layers.** The input shape is (N, c, ℓ) with batch size N , channels c , and signal length ℓ . BatchNorm estimates the mean $\hat{\mu}$ and variance $\hat{\sigma}^2$ over batch and time, and learns parameters (γ, β) to normalize the input. PSDNorm estimates PSDs $\hat{\mathbf{P}}$ over time and accounts for local temporal correlations. It computes the barycenter PSD $\hat{\mathbf{P}}$, updates it via a running Riemannian barycenter (11), and applies the filter $\hat{\mathbf{H}}$ to normalize the input. The hyperparameter f controls the extent of temporal correlation considered, thereby adjusting the strength of the normalization.

BatchNorm layers to mitigate data variability, employing a domain generalization approach: training a single model on a sufficiently diverse set of domains to ensure it generalizes to unseen datasets without additional adaptation. While this strategy shows promising performance, it raises the question of whether the model could be further adapted to the specifics of new subjects without retraining.

Test-time Domain Adaptation Domain Adaptation methods have been proposed to address this issue and provide adaptation to new domains. Traditional DA methods typically align source and target data distributions in feature space during training (Sun & Saenko, 2016; Damodaran et al., 2018). In the context of sleep staging, DA has been used to address domain shifts (Eldele et al., 2021). However, this approach has limitations, as it requires access to the source domain for each new target DA. An alternative is test-time DA, where the model is adapted to the target domain during inference without requiring access to the source domain (Gnassounou et al., 2023). This approach offers greater flexibility, enabling clinical use of the model without retraining or sharing the source data.

Contributions In this work, we introduce the PSDNorm deep learning layer, a novel approach to address distribution shifts in machine learning for signals. PSDNorm leverages Monge Mapping to incorporate temporal context and normalize feature maps effectively. As a test-time DA method, it adapts to distribution shifts during inference without extra training or source domain access. Compared to a nor-

malization like LayerNorm or InstanceNorm, PSDNorm exploits the sequential nature of the intermediate layer representations as illustrated in Figure 1. We evaluate PSDNorm through extensive experiments on 10 sleep staging datasets. PSDNorm achieves state-of-the-art performance and requires 4 times fewer labeled data to match the accuracy of the best baseline. Moreover, it improves robustness with higher F1 scores for the 20% most challenging subjects, proving its effectiveness against domain shifts. Results highlight the potential of PSDNorm as a practical and efficient solution for tackling domain shifts in signals. The paper is structured as follows: Section 2 discusses the U-Time model and existing normalization layers and pre-processing. Section 3 introduces PSDNorm, followed by numerical results in Section 4.

Notations Vectors are denoted by small cap boldface letters (e.g., \mathbf{x}), matrices by large cap boldface letters (e.g., \mathbf{X}). The element-wise product, power of n and division are \odot , \odot^n and \oslash , respectively. $\llbracket 1, K \rrbracket$ denotes $\{1, \dots, K\}$. The absolute value is $|\cdot|$. The discrete circular convolution along the temporal axis operates row-wise as, $* : \mathbb{R}^{c \times \ell} \times \mathbb{R}^{c \times f} \rightarrow \mathbb{R}^{c \times \ell}$ for $\ell \geq f$. $\text{vec} : \mathbb{R}^{c \times \ell} \rightarrow \mathbb{R}^{cl}$ concatenates rows of a time series into a vector. $x_l = [\mathbf{x}]_l$ refers to the l^{th} element of \mathbf{x} , and $X_{l,m} = [\mathbf{X}]_{l,m}$ denotes the element of \mathbf{X} at the l^{th} row and m^{th} column. \mathbf{X}^* and \mathbf{X}^\top are the conjugate and the transpose of \mathbf{X} , respectively. diag puts the elements of a vector on the diagonal of a matrix. \otimes is the Kronecker product. $\mathbf{1}_c$ is the vector of ones of size c .

2. Related Works

In this section, we first present U-Time (Perslev et al., 2019; 2021), a convolutional deep learning model designed for temporal sequence segmentation. Then, we review fundamental concepts of normalization layers with the BatchNorm (Ioffe & Szegedy, 2015) and InstanceNorm (Ulyanov, 2016) layers. Finally, we recall the Temporal Monge Alignment (TMA) method (Gnassounou et al., 2023) that aligns the PSD of signals using optimal transport.

2.1. U-Time: CNN for time series segmentation

U-Time (Perslev et al., 2019; 2021) is a convolutional neural network (CNN) inspired by the U-Net architecture (Ronneberger et al., 2015), designed for segmenting temporal sequences. U-Time maps sequential inputs of arbitrary length to sequences of class labels on a freely chosen temporal scale. The architecture is composed of several encoder and decoder blocks, with skip connections between them.

Encoder blocks A single encoder block is composed of a convolutional layer, an activation function, a BatchNorm layer, and a max pooling layer. First, the convolution is applied to the input signal, followed by the activation function and the BatchNorm layer. Finally, the max pooling layer downsamples the temporal dimension. In the following, the pre-BatchNorm feature map is denoted \mathbf{G} and the post-BatchNorm feature map $\widetilde{\mathbf{G}}$, *i.e.*, $\widetilde{\mathbf{G}} \triangleq \text{BatchNorm}(\mathbf{G})$. Each encoder block downsample by 2 the signal length but increases the number of channels.

Decoder blocks and Segmentation Head The decoding part of U-Time is symmetrical to the encoding part. Each decoder block doubles the signal length and decreases the number of channels. It is composed of a convolutional layer, an activation function, a BatchNorm layer, an upsampling layer and a concatenation layer of the skip connection of the corresponding encoding block. Finally, the segmentation head applies two convolutional layers with an activation function in between to output the final segmentation. It should be noted that U-Time employs BatchNorm layers but other normalization layers, such as LayerNorm (Ba et al., 2016) or InstanceNorm (Ulyanov, 2016) are possible.

2.2. Normalization Layers

Over the last decade, numerous normalization layers have been proposed to improve the training and robustness of deep neural networks. Among them, the BatchNorm (Ioffe & Szegedy, 2015), InstanceNorm (Ulyanov, 2016), and LayerNorm (Ba et al., 2016) layers are the most popular. We present the first two as they are routinely used in deep learning models for time series processing, and illustrate them in Figure 1.

BatchNorm The BatchNorm layer (Ioffe & Szegedy, 2015) normalizes features maps in a neural network to have zero mean and unit variance. At train time, given a batch $\mathcal{B} = \{\mathbf{G}^{(1)}, \dots, \mathbf{G}^{(N)}\} \subset \mathbb{R}^{c \times \ell}$ of N pre-BatchNorm feature maps and for all $j, m, l \in \llbracket 1, N \rrbracket \times \llbracket 1, c \rrbracket \times \llbracket 1, \ell \rrbracket$, the BatchNorm layer is computed as

$$\widetilde{G}_{m,l}^{(j)} = \gamma_m \frac{G_{m,l}^{(j)} - \widehat{\mu}_m}{\sqrt{\widehat{\sigma}_m^2 + \varepsilon}} + \beta_m, \quad (1)$$

where $\gamma, \beta \in \mathbb{R}^c$ are learnable parameters. The mean and standard deviation $\widehat{\mu} \in \mathbb{R}^c$ and $\widehat{\sigma} \in \mathbb{R}^c$ are computed across the time and the batch,

$$\begin{aligned} \widehat{\mu}_m &\triangleq \frac{1}{N\ell} \sum_{j=1}^N \sum_{l=1}^{\ell} G_{m,l}^{(j)}, \\ \widehat{\sigma}_m^2 &\triangleq \frac{1}{N\ell} \sum_{j=1}^N \sum_{l=1}^{\ell} (G_{m,l}^{(j)} - \widehat{\mu}_m)^2. \end{aligned} \quad (2)$$

At test time, the mean and variance $\widehat{\mu}$ and $\widehat{\sigma}$ are replaced by their running mean and variance, also called exponential moving average, estimated during training.

InstanceNorm and RevIN Another popular normalization is the InstanceNorm layer (Ulyanov, 2016). During training, InstanceNorm operates similarly to (1), but the mean and variance are computed per sample instead of across the batch dimension, *i.e.*, $\widehat{\mu}_m^{(j)}$ and $\widehat{\sigma}_m^{(j)}$ are computed for each sample j ,

$$\begin{aligned} \widehat{\mu}_m^{(j)} &\triangleq \frac{1}{\ell} \sum_{l=1}^{\ell} G_{m,l}^{(j)}, \\ (\widehat{\sigma}_m^{(j)})^2 &\triangleq \frac{1}{\ell} \sum_{l=1}^{\ell} (G_{m,l}^{(j)} - \widehat{\mu}_m^{(j)})^2. \end{aligned} \quad (3)$$

Hence, each sensor of each sample is normalized independently of the others. At test time, InstanceNorm behaves identically to its training phase and therefore does not rely on running statistics contrary to the BatchNorm. This layer has seen a growing interest for time-series forecasting with the RevIN layer (Kim et al., 2021) which applies InstanceNorm during the encoding and then reverses the normalization during the decoding to generate the forecast.

2.3. Power Spectral Density Alignment

Traditional normalization techniques, such as those discussed above, adjust statistical properties without accounting for the temporal structure of the data. To address this limitation, the Temporal Monge Alignment (TMA) (Gnassounou et al., 2023; 2024) was introduced as a pre-processing step to align temporal correlations by leveraging the Power Spectral density (PSD) of multivariate signals using Monge Optimal Transport mapping.

Gaussian Periodic Signals Consider a multivariate signal $\mathbf{X} \triangleq [\mathbf{x}_1, \dots, \mathbf{x}_c]^\top \in \mathbb{R}^{c \times \ell}$ of sufficient length. A standard assumption is that this signal follows a centered Gaussian distribution where sensors are uncorrelated and signals are periodic. This periodicity and uncorrelation structure implies that the signal's covariance matrix is block diagonal, with each block having a circulant structure. A fundamental property of symmetric positive definite circulant matrices is their diagonalization (Gray, 2006) with real and positive eigenvalues in the Fourier basis $\mathbf{F}_\ell \in \mathbb{C}^{\ell \times \ell}$ of elements

$$[\mathbf{F}_\ell]_{l,l'} \triangleq \frac{1}{\sqrt{\ell}} \exp \left(-2i\pi \frac{(l-1)(l'-1)}{\ell} \right), \quad (4)$$

where $l, l' \in \llbracket 1, \ell \rrbracket$. Hence, we have $\text{vec}(\mathbf{X}) \sim \mathcal{N}(\mathbf{0}, \Sigma)$ with Σ block-diagonal,

$$\Sigma = (\mathbf{I}_c \otimes \mathbf{F}_\ell) \text{diag}(\text{vec}(\mathbf{P})) (\mathbf{I}_c \otimes \mathbf{F}_\ell^*) \in \mathbb{R}^{c\ell \times c\ell}, \quad (5)$$

where $\mathbf{P} \in \mathbb{R}^{c \times \ell}$ contains positive entries corresponding to the PSD of each sensor. In practice, since we only have access to a single realization of the signal, the PSD is estimated with only $f \ll \ell$ frequencies, *i.e.*, $\mathbf{P} \in \mathbb{R}^{c \times f}$. This amounts to considering the local correlation of the signal and neglecting the long-range correlations.

Power Spectral Density Estimation The Welch estimator (Welch, 1967) computes the PSD of a signal by averaging the squared Fourier transform of overlapping segments of the signal. Hence, the realization of the signal $\mathbf{X} \in \mathbb{R}^{c \times \ell}$ is decimated into overlapping segments $\{\mathbf{X}^{(1)}, \dots, \mathbf{X}^{(L)}\} \subset \mathbb{R}^{c \times f}$ to estimate the PSD. The Welch estimator is defined as

$$\hat{\mathbf{P}} \triangleq \frac{1}{L} \sum_{l=1}^L \left| \left((\mathbf{1}_c \mathbf{w}^\top) \odot \mathbf{X}^{(l)} \right) \mathbf{F}_f^* \right|^{\odot 2} \in \mathbb{R}^{c \times f}, \quad (6)$$

where $\mathbf{w} \in \mathbb{R}^f$ is the window function such that $\|\mathbf{w}\|_2 = 1$.

f -Monge Mapping Let $\mathcal{N}(\mathbf{0}, \Sigma^{(s)})$ and $\mathcal{N}(\mathbf{0}, \Sigma^{(t)})$ be source and target centered Gaussian distributions respectively with covariance matrices following the structure (5) and PSDs denoted by $\mathbf{P}^{(s)}$ and $\mathbf{P}^{(t)} \in \mathbb{R}^{c \times f}$. Given a signal $\mathbf{X} \in \mathbb{R}^{c \times \ell}$ such that $\text{vec}(\mathbf{X}) \sim \mathcal{N}(\mathbf{0}, \Sigma^{(s)})$, the f -Monge mapping as defined by Gnassounou et al. (2023; 2024) is

$$m_f(\mathbf{X}, \mathbf{P}^{(t)}) \triangleq \mathbf{X} * \mathbf{H} \in \mathbb{R}^{c \times \ell}, \quad (7)$$

where

$$\mathbf{H} \triangleq \frac{1}{\sqrt{f}} \left(\mathbf{P}^{(t)} \oslash \mathbf{P}^{(s)} \right)^{\odot \frac{1}{2}} \mathbf{F}_f^* \in \mathbb{R}^{c \times f}. \quad (8)$$

In this case, f controls the alignment between the source and target distributions. Indeed, if $f = \ell$, then the f -Monge mapping is the classical Monge mapping between Gaussian distributions and the source signal has its covariance matrix equal to $\Sigma^{(t)}$ after the mapping. If $f = 1$, then each sensor is only multiplied by a scalar.

Gaussian Wasserstein Barycenter For Gaussian distributions admitting the decomposition (5), the Wasserstein barycenter (Aguech & Carlier, 2011) admits an elegant closed-form solution. Consider K centered Gaussian distributions admitting the decomposition (5) of PSDs $\mathbf{P}^{(1)}, \dots, \mathbf{P}^{(K)}$. Their barycenter is also a centered Gaussian distribution $\mathcal{N}(\mathbf{0}, \bar{\Sigma})$ admitting the decomposition (5) with PSD

$$\bar{\mathbf{P}} \triangleq \left(\frac{1}{K} \sum_{k=1}^K \mathbf{P}^{(k)}^{\odot \frac{1}{2}} \right)^{\odot 2} \in \mathbb{R}^{c \times f}. \quad (9)$$

Temporal Monge Alignment TMA is a pre-processing method that aligns the PSD of multivariate signals using the f -Monge mapping. Given a source signal \mathbf{X}_s and a set of target signals $\mathbf{X}_t = \{\mathbf{X}_t^{(1)}, \dots, \mathbf{X}_t^{(K)}\}$, the TMA method uses the f -Monge mapping between the source and the Wasserstein barycenter of the target signals. Hence, it simply consists of 1) estimating the PSD of all the signals, 2) computing the Wasserstein barycenter of the target signals, and 3) applying the f -Monge mapping to the source signal. TMA, as a preprocessing method, is inherently limited to handling PSD shifts in the raw signals and cannot address more complex distributional changes in the data. This limitation highlights the need for a layer that can effectively capture and adapt to these complex variations during learning and inside deep learning models.

3. PSDNorm Layer

The classical normalization layers, such as BatchNorm or InstanceNorm do not take into account the temporal autocorrelation structure of signals. They treat each time sample in the intermediate representations independently. In this section, we introduce the PSDNorm layer that aligns the PSD of each signal onto a barycenter PSD within the architecture of a deep learning model.

PSDNorm as a Drop-in Replacement As discussed in Section 2, BatchNorm and InstanceNorm layers are commonly applied after each non-linearity in deep learning models, such as U-Time, to normalize feature maps. In contrast, PSDNorm offers a novel approach by aligning the PSD of feature maps to a barycenter PSD, providing a powerful alternative to classical normalization layers. Designed as a drop-in replacement, PSDNorm is optimized for modern hardware accelerators like GPUs, ensuring efficient execution. Once the deep-learning model is trained, PSDNorm operates as a test-time domain adaptation technique, allowing it to adapt to new data without additional training or access to training data. We define the normalized feature map as $\tilde{\mathbf{G}} \triangleq \text{PSDNorm}(\mathbf{G})$. The following sections introduce the core components of PSDNorm and its implementation.

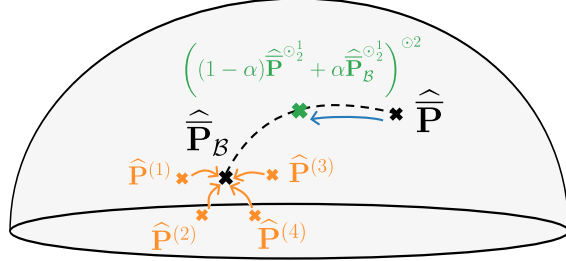


Figure 2: **Description of the running Riemannian barycenter.** The barycenter of the batch $\hat{\mathbf{P}}_B$ is estimated from the PSD of each batch sample. Then the running Riemannian barycenter is updated through an exponential average along the geodesic (- -), parameterized by $\alpha \in [0, 1]$.

3.1. Core Components of the layer

In the following, we formally define PSDNorm and present each of its three main components: 1) PSD estimation, 2) running Riemannian barycenter estimation, and 3) f -Monge mapping computation. Given a batch $\mathcal{B} = \{\mathbf{G}^{(1)}, \dots, \mathbf{G}^{(N)}\}$ of N pre-normalization feature maps, PSDNorm outputs a normalized batch $\tilde{\mathcal{B}} = \{\tilde{\mathbf{G}}^{(1)}, \dots, \tilde{\mathbf{G}}^{(N)}\}$ with normalized PSD. Those three steps are detailed in the following and illustrated in the right part of Figure 1.

PSD Estimation First, the estimation of the PSD of each feature map is performed using the Welch method. The per-channel mean $\hat{\mu}^{(j)}$ is computed for each feature map $\mathbf{G}^{(j)}$ as

$$\hat{\mu}^{(j)} \triangleq \frac{1}{\ell} \sum_{l=1}^{\ell} [\mathbf{G}^{(j)}]_{:,l} \in \mathbb{R}^c. \quad (10)$$

Then, the PSD of the centered feature map $\mathbf{G}^{(j)} - \hat{\mu}^{(j)}\mathbf{1}_{\ell}^{\top}$, denoted $\hat{\mathbf{P}}^{(j)}$, is estimated as described in Equation (6). This centering step is required as feature maps are typically non-centered due to activation functions and convolution biases but they are assumed to have a stationary mean. The Welch estimation involves segmenting the centered feature map into overlapping windows, computing the Fourier transform of each window and then averaging them.

Geodesic and Running Riemannian Barycenter The PSDNorm aligns the PSD of each feature map to a barycenter PSD. This barycenter is computed during training by interpolating between the batch Wasserstein barycenter and the current running Riemannian barycenter using the geodesic associated with the Bures metric (Bhatia et al., 2019). The batch barycenter is first computed from the current batch PSDs $\{\hat{\mathbf{P}}^{(1)}, \dots, \hat{\mathbf{P}}^{(N)}\}$ using Equation (9). To ensure gradual adaptation, the running barycenter is updated via an

Algorithm 1 Forward pass of PSDNorm

```

1: Input: Batch  $\mathcal{B} = \{\mathbf{G}^{(1)}, \dots, \mathbf{G}^{(N)}\}$ , running
   barycenter  $\hat{\mathbf{P}}$ , filter-size  $f$ , momentum  $\alpha$ , training flag
2: Output: Normalized batch  $\{\tilde{\mathbf{G}}^{(1)}, \dots, \tilde{\mathbf{G}}^{(N)}\}$ 
3: for  $j = 1$  to  $N$  do
4:    $\hat{\mu}^{(j)} \leftarrow$  Mean estimation with eq. (10)
5:    $\hat{\mathbf{P}}^{(j)} \leftarrow$  PSD est. from  $\tilde{\mathbf{G}}^{(j)} - \hat{\mu}^{(j)}\mathbf{1}_{\ell}^{\top}$  with eq. (6)
6: end for
7: if training then
8:    $\hat{\mathbf{P}}_B \leftarrow$  Batch bary. from  $\{\hat{\mathbf{P}}^{(j)}\}_j$  with eq. (9)
9:    $\hat{\mathbf{P}} \leftarrow$  Running bary. up. from  $\hat{\mathbf{P}}, \hat{\mathbf{P}}_B$  with eq. (11)
10: end if
11: for  $j = 1$  to  $N$  do
12:    $\hat{\mathbf{H}}^{(j)} \leftarrow$  Filter estimation from  $\hat{\mathbf{P}}^{(j)}, \hat{\mathbf{P}}$  with eq. (13)
13:    $\tilde{\mathbf{G}}^{(j)} \leftarrow$   $f$ -Monge mapping with eq. (12)
14: end for

```

exponential geodesic average with $\alpha \in [0, 1]$:

$$\hat{\mathbf{P}} \leftarrow \left((1 - \alpha)\hat{\mathbf{P}}^{\odot \frac{1}{2}} + \alpha\hat{\mathbf{P}}_B^{\odot \frac{1}{2}} \right)^{\odot 2} \in \mathbb{R}^{c \times f}. \quad (11)$$

A proof of the geodesic is provided in Appendix A.2.

PSD Adaptation with f -Monge Mapping The final step of the PSDNorm is the application of the f -Monge mapping to each feature map after subtracting the per-channel mean. Indeed, for all $j \in \llbracket 1, N \rrbracket$, it is defined as

$$\begin{aligned} \tilde{\mathbf{G}}^{(j)} &= m_f \left(\mathbf{G}^{(j)} - \hat{\mu}^{(j)}\mathbf{1}_{\ell}^{\top}, \hat{\mathbf{P}} \right) \\ &= \left(\left(\mathbf{G}^{(j)} - \hat{\mu}^{(j)}\mathbf{1}_{\ell}^{\top} \right) * \hat{\mathbf{H}}^{(j)} \right) \in \mathbb{R}^{c \times \ell} \end{aligned} \quad (12)$$

where $\hat{\mathbf{H}}^{(j)}$ is the Monge mapping filter computed as

$$\hat{\mathbf{H}}^{(j)} \triangleq \frac{1}{\sqrt{f}} \left(\hat{\mathbf{P}} \oslash \hat{\mathbf{P}}^{(j)} \right)^{\odot \frac{1}{2}} \mathbf{F}_f^* \in \mathbb{R}^{c \times f} \quad (13)$$

where $\hat{\mathbf{P}}^{(j)}$ is the estimated PSD of $\mathbf{G}^{(j)} - \hat{\mu}^{(j)}\mathbf{1}_{\ell}^{\top}$.

3.2. Implementation details

Overall Algorithm The forward computation of the proposed layer is outlined in Algorithm 1. At train time, the PSDNorm performs three main operations: 1) PSD estimation, 2) running Riemannian barycenter update, and 3) Monge mapping application. At test time, the PSDNorm operates similarly, except it does not update the running barycenter. The PSDNorm is fully differentiable and can be integrated into any deep learning model. Similarly to classical normalization layers, a stop gradient operation is applied to the running barycenter to prevent the backpropagation of the gradient computation through the barycenter.

Filter Size and Computational Complexity PSDNorm has a unique additional hyperparameter f which is the filter size. It controls the alignment between each feature map and the running barycenter PSD and it is typically chosen in $\{16, 32, 64\}$. In practice, Fourier transforms are computed using the Fast Fourier Transform (FFT) algorithm. Because of the estimation of PSDs, the complexity of the PSDNorm, both at train and test times, is $\mathcal{O}(Nclf \log(f))$, where N is the batch size, c the number of channels, l the signal length, and f the filter size.

4. Numerical Experiments

In this section, we evaluate the proposed method through a series of experiments designed to highlight its effectiveness and robustness. We first describe the datasets and training setup employed in our study, followed by a performance comparison with existing normalization techniques. Next, we assess the robustness of PSDNorm by focusing on its performance over the hardest subjects in the datasets. Finally, we assess its data efficiency under varying training set sizes. The code will be available on github upon acceptance. The anonymized code is available in the supplementary material.

4.1. Experimental Setup

Datasets To evaluate the effect of normalization layers, we use ten datasets of sleep staging described in Table 1. ABC (Jessie P. et al., 2018), CCSHS (Rosen et al., 2003), CFS (Redline et al., 1995), HPAP (Rosen et al., 2012), MROS (Blackwell et al., 2011), SHHS (Quan et al., 1998), CHAT (Marcus et al., 2013), and SOF (Spira et al., 2008) are publicly available sleep datasets with restricted access from National Sleep Research Resource (NSRR) (Zhang et al., 2018). PHYS (Goldberger et al., 2000) and MASS (O'Reilly et al., 2014) are two other datasets publicly available. Every 30 s epoch is labeled with one of the five sleep stages: Wake, N1, N2, N3, and REM. These datasets are unbalanced in terms of age, sex, number of subjects, and have been recorded with different sensors in different institutions which makes the sleep staging task challenging. We now describe the pre-processing steps and splits of the datasets.

Data Pre-processing The pre-processing pipeline is widely used in the field (Chambon et al., 2017; Stephansen et al., 2018). The datasets vary in the number and type of available EEG and electrooculogram (EOG) channels. To ensure consistency, we use two bipolar EEG channels, as some datasets lack additional channels. For dataset from NSRR, we select the channels C3-A2 and C4-A1. For signals from Physionet and MASS, we use the only available channels Fpz-Cz and Pz-Oz. The EEG signals are low-pass filtered with a 30 Hz cutoff frequency and resampled to 100 Hz. All data extraction and pre-processing steps are

Table 1: **Characteristics of the datasets used in the experiments.** The 10 sleep-staging datasets are divided into 7 training datasets, where some subjects are left out for validation and testing, and 3 test datasets that remain entirely unseen during training. Each training dataset is further split into training (64% of subjects), validation (16%), and test (20%) sets.

	Dataset	Subjects	Records	Age \pm std	Sex % (F/M)
Train	ABC	44	117	48.8 \pm 9.8	43/57
	CCSHS	231	231	17.7 \pm 0.4	50/50
	CFS	681	682	41.7 \pm 20.0	55/45
	HPAP	147	147	46.5 \pm 11.9	43/57
	MROS	1631	1631	76.4 \pm 5.5	0/100
	PHYS	70	132	58.8 \pm 22.0	33/67
	SHHS	792	919	63.1 \pm 11.2	52/48
Test	MASS	61	61	42.5 \pm 18.9	55/45
	CHAT	1230	1635	6.6 \pm 1.4	52/48
	SOF	434	434	82.8 \pm 3.1	100/0

implemented using MNE-BIDS (Appelhoff et al., 2019) and MNE-Python (Gramfort et al., 2013).

Dataset Split The datasets in Table 1 are divided into train (upper part) and test (lower part) groups. The training datasets are used for both training and testing (with left-out subjects), while the test datasets serve only for testing, *i.e.*, are unseen during training. This split allows us to evaluate the model's generalization across diverse age groups, sex distributions, and sensors placements. CHAT focuses on children, SOF on elderly women, and MASS on adults. Training datasets are divided into training, validation, and testing sets with a 64%/16%/20% subject split. All experiments are conducted using this split.

Architecture and Training Several architectures have been proposed in the literature for sleep staging (Chambon et al., 2017; Stephansen et al., 2018; Phan et al., 2022; 2023). In this work, we use the U-Sleep architecture (Perslev et al., 2021), a state-of-the-art variant of the U-Time model designed for large-scale training and robustness across datasets. The used implementation is from the Braindecode library (Schirrmeister et al., 2017). We use the Adam optimizer (Kingma, 2014), with a learning rate of 10^{-3} , to minimize the cross-entropy loss. The batch size is set to 64 and the early stopping is done on the validation set with a patience of 5 epochs. The inputs are sequences of 17'30s with a stride of 5' of the full night recording.

Evaluation During testing, the model processes sequences of 17'30s with a stride of 5'. Performance is evaluated using the weighted F1 score, computed on the central 7'30s prediction of the sequence to minimize edge effects.

Table 2: **Scores of different methods on the left-out subjects from the training datasets and the full test datasets.** (Left) F1 score across all subjects. (Right) F1@20% score, representing the F1 score for the 20% lowest-performing subjects. The upper section displays results for training datasets with subject left-out *i.e.*, **small shift**, while the lower section presents results for testing datasets (unseen at training) *i.e.*, **large shift**. The best scores are highlighted in **bold**. N/A means too few subjects to compute the F1@20%. The reported standard deviations indicate performance variability across subjects.

		F1 Score				F1@20% Score			
		BatchNorm	InstanceNorm	TMA	PSDNorm	BatchNorm	InstanceNorm	TMA	PSDNorm
Train	ABC	0.79 ± 0.06	0.79 ± 0.06	0.70 ± 0.08	0.78 ± 0.08	N/A	N/A	N/A	N/A
	CCSHS	0.91 ± 0.04	0.90 ± 0.05	0.86 ± 0.07	0.91 ± 0.04	0.85 ± 0.03	0.84 ± 0.02	0.80 ± 0.09	0.85 ± 0.03
	CFS	0.90 ± 0.06	0.89 ± 0.06	0.86 ± 0.08	0.89 ± 0.06	0.80 ± 0.08	0.81 ± 0.07	0.77 ± 0.10	0.80 ± 0.08
	HOMEPA	0.80 ± 0.08	0.80 ± 0.08	0.75 ± 0.09	0.79 ± 0.08	0.69 ± 0.05	0.70 ± 0.05	0.63 ± 0.10	0.67 ± 0.06
	MROS	0.89 ± 0.05	0.89 ± 0.05	0.87 ± 0.06	0.89 ± 0.05	0.81 ± 0.06	0.81 ± 0.05	0.79 ± 0.07	0.81 ± 0.05
	PhysioNet	0.84 ± 0.05	0.82 ± 0.07	0.69 ± 0.08	0.83 ± 0.05	0.75 ± 0.04	0.70 ± 0.07	0.67 ± 0.07	0.75 ± 0.00
	SHHS	0.87 ± 0.06	0.87 ± 0.06	0.80 ± 0.13	0.87 ± 0.06	0.77 ± 0.05	0.79 ± 0.06	0.68 ± 0.12	0.78 ± 0.06
Test	CHAT	0.75 ± 0.09	0.76 ± 0.09	0.74 ± 0.10	0.79 ± 0.07	0.61 ± 0.07	0.64 ± 0.08	0.69 ± 0.12	0.70 ± 0.07
	MASS	0.74 ± 0.11	0.76 ± 0.10	0.54 ± 0.14	0.79 ± 0.08	0.58 ± 0.07	0.63 ± 0.11	0.49 ± 0.13	0.70 ± 0.07
	SOF	0.86 ± 0.06	0.86 ± 0.06	0.83 ± 0.09	0.86 ± 0.06	0.76 ± 0.06	0.76 ± 0.05	0.72 ± 0.11	0.76 ± 0.06

Normalization Strategies We compare the proposed PSDNorm with three normalization strategies: TMA pre-processing, BatchNorm, and InstanceNorm. TMA is applied as a pre-processing step while retaining BatchNorm in the architecture. Alternatively, BatchNorm layers are replaced in the first three convolutional layers with either PyTorch’s InstanceNorm (Paszke et al., 2019) (using default parameters) or PSDNorm. To preserve the receptive field, the filter size of PSDNorm is set to f in the first layer and progressively halved in subsequent layers. Except for the sensitivity analysis, f is set to 16 and α to 10^{-2} . A detailed analysis of the neural network depth at which PSDNorm is applied is provided in the supplementary material (Appendix A.1).

4.2. Numerical results

In this sub-section, we present the results of the experiments to evaluate the effectiveness of PSDNorm. We compare its performance against the other normalization strategies on the test sets of the training datasets and the full test datasets. Then, we assess the robustness of PSDNorm by focusing on its performance over the hardest subjects in the datasets. We also analyze the data efficiency of PSDNorm by examining its performance with different training set sizes. Finally, the sensitivity of the filter size is investigated to understand its impact on the model’s performance.

Performance Comparison: Training & Testing Datasets

The left part of the Table 2 presents the F1 scores across the different datasets, highlighting the impact of different normalization strategies under varying distribution shifts. For training datasets, where distribution shifts are relatively small, TMA consistently underperforms compared to other normalization layers, with F1 scores ranging from 2% (MROS) to 15% (PhysioNet) lower. This suggests that applying strong pre-processing with a powerful network like

U-Sleep is detrimental. In contrast, all normalization layers achieve comparable results, with F1 scores within 1% of each other. On testing datasets, which exhibit larger distribution shifts, PSDNorm outperforms all baselines, particularly on CHAT and MASS, where it improves over the best alternative by at least 3%. Notably, PSDNorm surpasses BatchNorm by 4% and 5% on CHAT and MASS, demonstrating its effectiveness in handling distribution shifts. On SOF, all normalization layers perform similarly, except for TMA, which shows lower performance. These results demonstrate the effectiveness of PSDNorm in handling distribution shifts, emphasizing that incorporating temporal structure into normalization is crucial for achieving robust and generalizable performance across test datasets.

Robustness: Performance over Most Challenging Subjects

Performance variability across subjects is a key challenge in biomedical applications where ensuring consistently high performance—even for the most challenging subjects—is critical. To evaluate model robustness, we use the F1@20% score (Gnassounou et al., 2023), which measures performance on the 20% of subjects with the lowest F1 scores under the BatchNorm baseline. Across all datasets and methods, performance drops significantly for the hardest subjects compared to all subjects, highlighting the difficulty of the task. TMA performs the worst, reinforcing that strong pre-processing can be detrimental when dealing with subject variability. PSDNorm demonstrates a strong improvement over BatchNorm, achieving a 9% and 12% increase in F1@20% on CHAT and MASS, respectively. Compared to InstanceNorm, PSDNorm provides an important increase, with 6% and 7% improvements on CHAT and MASS. These results show the benefit of using temporal structure for normalization, especially for handling the hardest subjects. On SOF, all normalization methods perform similarly, as expected, given that BatchNorm al-

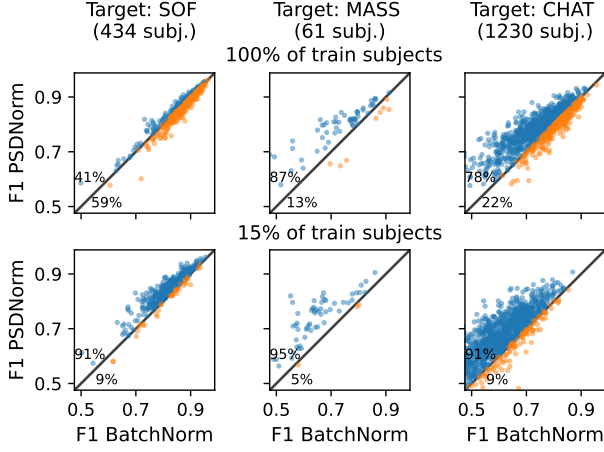


Figure 3: **Subject-wise F1 score comparison between BatchNorm and PSDNorm across test datasets and training set sizes.** F1 score of each subject with BatchNorm (x-axis) are plotted against those with PSDNorm (y-axis). The top row shows training with 15% of subjects, the bottom with 100%. Dots are blue when the performance is improved with PSDNorm and orange when it is decreased.

ready achieves high performance on this dataset.

To better highlight the robustness of PSDNorm, Figure 3 presents a scatter plot of subject-wise F1 scores comparing BatchNorm and PSDNorm across different target datasets (upper row). PSDNorm improves performance for 87% of subjects in MASS and 78% in CHAT, with the largest gains observed for the hardest subjects, reinforcing its ability to handle challenging cases.

Data Efficiency: Effect of Training Set Size In many real-world scenarios, especially in biomedical applications, labeled data can be limited and expensive to collect, or simply not available for privacy reasons. This experiment assesses the data efficiency of PSDNorm by analyzing how performance scales with the number of training subjects, determining whether it can achieve strong results with fewer samples. To do so, we vary the percentage of subjects used for training across different datasets while maintaining the original dataset distribution. For each percentage, we perform three random splits and report the average F1 score to ensure robustness. Figure 4 illustrates the impact of training set size on the performance of PSDNorm with different f values, as well as BatchNorm. As expected, performance improves with more training subjects. Furthermore, PSDNorm significantly outperforms BatchNorm in small-data settings, especially for larger f , where the normalization effect is stronger. At 15% of subjects, PSDNorm achieves an average F1 score of 77% on test datasets, compared to 66% for BatchNorm, demonstrating its superior ability to learn from limited data. Overall, PSDNorm requires four times

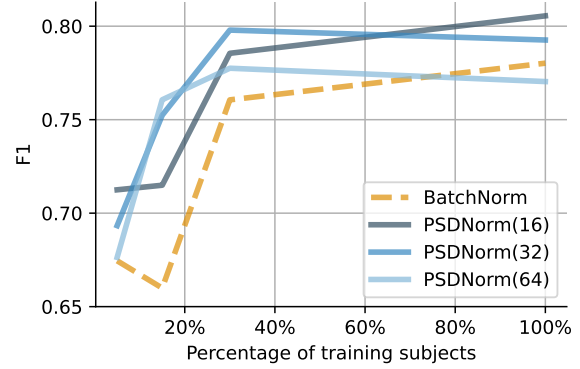


Figure 4: **Impact of the number of training subjects on the test datasets F1 score.** F1 score is computed on the test datasets (*i.e.*, **large shift**) for BatchNorm (dashed orange line) and PSDNorm with different numbers of components, $f \in \{16, 32, 64\}$.

fewer subjects to reach the same performance as BatchNorm trained on the full dataset. Figure 3 further highlights this improvement, showing that with only 15% of training subjects, PSDNorm enhances performance for 91% of subjects in SOF, 95% in MASS, and 91% in CHAT, confirming its effectiveness in small-data scenarios.

Sensitivity to Filter Size The choice of f in PSDNorm controls the intensity of the normalization: larger f provide stronger normalization, while smaller f allow more flexibility in the model. In Figure 4, we evaluate its impact across different training set sizes and observe a clear trend: when trained on fewer subjects, larger filter sizes yield better performance, whereas smaller filter sizes are more effective with larger datasets. This suggests that with limited data, stronger normalization is beneficial to avoid overfitting, while with more data, a more flexible model is preferred.

5. Conclusion

In this paper, we introduced PSDNorm, a novel normalization layer for deep neural networks that aligns the power spectral density (PSD) of each signal to a geodesic barycenter at every layer where it is applied. Through extensive experiments on multiple sleep staging datasets, we demonstrated that PSDNorm not only enhances performance but also improves robustness and data efficiency, outperforming existing normalization techniques such as BatchNorm, and InstanceNorm.

Beyond time-series, its adaptability makes it a promising candidate for broader tasks, such as audio analysis, images and videos with high variability in the data distribution.

Impact Statement

We believe our work advances Machine Learning by introducing a test-time adaptation method that improves robustness to distribution shifts, particularly in biomedical applications such as EEG analysis. By leveraging temporal context, our approach enables finer subject-specific adjustments, leading to more accurate and reliable predictions. Furthermore, since adaptation occurs at test time without requiring additional training data, our method helps preserve data privacy, making it well-suited for deployment in sensitive biomedical settings.

Acknowledgements

This work was supported by the grants ANR-22-PESN-0012 to AC under the France 2030 program, ANR-20-CHIA-0016 and ANR-20-IADJ-0002 to AG while at Inria, and ANR-23-ERCC-0006 to RF, all from Agence nationale de la recherche (ANR). This project has also received funding from the European Union's Horizon Europe research and innovation programme under grant agreement 101120237 (ELIAS).

All the datasets used for this work were accessed and processed on the Inria compute infrastructures.

Numerical computation was enabled by the scientific Python ecosystem: Matplotlib (Hunter, 2007), Scikit-learn (Pedregosa et al., 2011), Numpy (Harris et al., 2020), Scipy (Virtanen et al., 2020), PyTorch (Paszke et al., 2019) and MNE (Gramfort et al., 2013).

References

Aguech, M. and Carlier, G. Barycenters in the wasserstein space. *SIAM Journal on Mathematical Analysis*, 43(2): 904–924, 2011.

Apicella, A., Isgrò, F., Pollastro, A., and Prevete, R. On the effects of data normalization for domain adaptation on EEG data. *Engineering Applications of Artificial Intelligence*, 123:106205, 2023.

Appelhoff, S., Sanderson, M., Brooks, T. L., van Vliet, M., Quentin, R., Holdgraf, C., Chaumon, M., Mikulan, E., Tavabi, K., Höchenberger, R., Welke, D., Brunner, C., Rockhill, A. P., Larson, E., Gramfort, A., and Jas, M. MNE-BIDS: Organizing electrophysiological data into the BIDS format and facilitating their analysis. *Journal of Open Source Software*, 4(44):1896, 2019. doi: 10.21105/joss.01896.

Ba, J. L., Kiros, J. R., and Hinton, G. E. Layer normalization, 2016. URL <http://arxiv.org/abs/1607.06450>.

Bhatia, R., Jain, T., and Lim, Y. On the bures–wasserstein distance between positive definite matrices. *Expositiones Mathematicae*, 37(2):165–191, 2019.

Blackwell, T., Yaffe, K., Ancoli-Israel, S., Redline, S., Ensrud, K. E., Stefanick, M. L., Laffan, A., Stone, K. L., and Osteoporotic Fractures in Men Study Group. Associations between sleep architecture and sleep-disordered breathing and cognition in older community-dwelling men: the Osteoporotic Fractures in Men Sleep Study. *Journal of the American Geriatrics Society*, 59(12): 2217–2225, December 2011. ISSN 1532-5415. doi: 10.1111/j.1532-5415.2011.03731.x.

Chambon, S., Galtier, M., Arnal, P., Wainrib, G., and Gramfort, A. A deep learning architecture for temporal sleep stage classification using multivariate and multimodal time series. 2017.

Chambon, S., Galtier, M. N., Arnal, P. J., Wainrib, G., and Gramfort, A. A deep learning architecture for temporal sleep stage classification using multivariate and multimodal time series. *IEEE Transactions on Neural Systems and Rehabilitation Engineering*, 26(4):758–769, 2018.

Damodaran, B. B., Kellenberger, B., Flamary, R., Tuia, D., and Courty, N. Deepjdot: Deep joint distribution optimal transport for unsupervised domain adaptation. In *Proceedings of the European conference on computer vision (ECCV)*, pp. 447–463, 2018.

Eldele, E., Ragab, M., Chen, Z., Wu, M., Kwoh, C., Li, X., and Guan, C. Adast: Attentive cross-domain EEG-based sleep staging framework with iterative self-training. *IEEE Transactions on Emerging Topics in Computational Intelligence*, 7:210–221, 2021.

Gnassounou, T., Flamary, R., and Gramfort, A. Convolutional monge mapping normalization for learning on biosignals. In *Neural Information Processing Systems (NeurIPS)*, 2023.

Gnassounou, T., Collas, A., Flamary, R., Lounici, K., and Gramfort, A. Multi-source and test-time domain adaptation on multivariate signals using spatio-temporal monge alignment. *arXiv preprint arXiv:2407.14303*, 2024.

Goldberger, A., Amaral, L., Glass, L., Havlin, S., Hausdorff, J., Ivanov, P., Mark, R., Mietus, J., Moody, G., Peng, C.-K., Stanley, H., and Physiobank, P. Components of a new research resource for complex physiologic signals. *PhysioNet*, 101, 01 2000.

Gramfort, A., Luessi, M., Larson, E., Engemann, D. A., Strohmeier, D., Brodbeck, C., Goj, R., Jas, M., Brooks, T., Parkkonen, L., and Hämäläinen, M. S. MEG and EEG data analysis with MNE-Python. *Frontiers in Neuroscience*, 7(267):1–13, 2013. doi: 10.3389/fnins.2013.00267.

Gray, R. M. Toeplitz and circulant matrices: A review. *Foundations and Trends® in Communications and Information Theory*, 2(3):155–239, 2006. ISSN 1567-2190. doi: 10.1561/0100000006. URL <http://dx.doi.org/10.1561/0100000006>.

Guillot, A. and Thorey, V. RobustSleepNet: Transfer learning for automated sleep staging at scale. 2021.

Harris, C., Millman, K., van der Walt, S., Gommers, R., Virtanen, P., Cournapeau, D., Wieser, E., Taylor, J., Berg, S., Smith, N., Kern, R., Picus, M., Hoyer, S., van Kerkwijk, M., Brett, M., Haldane, A., del Río, J. F., Wiebe, M., Peterson, P., G'erard-Marchant, P., Sheppard, K., Reddy, T., Weckesser, W., Abbasi, H., Gohlke, C., and Oliphant, T. Array programming with NumPy. *Nature*, 585(7825):357–362, 2020.

Hunter, J. D. Matplotlib: A 2d graphics environment. *Computing in science & engineering*, 9(3):90–95, 2007.

Ioffe, S. and Szegedy, C. Batch normalization: accelerating deep network training by reducing internal covariate shift. In *Proceedings of the 32nd International Conference on International Conference on Machine Learning - Volume 37*, ICML'15, pp. 448–456. JMLR.org, 2015.

Jessie P., B., Ali, T., Michael, R., Wei, W., Robert, A., Atul, M., Robert L., O., Amit, A., Katherine, D., and Sanya R., P. Gastric Banding Surgery versus Continuous Positive Airway Pressure for Obstructive Sleep Apnea: A Randomized Controlled Trial. *American journal of respiratory and critical care medicine*, 197(8), April 2018. ISSN 1535-4970. doi: 10.1164/rccm.201708-1637LE. URL <https://pubmed.ncbi.nlm.nih.gov/29035093/>. Publisher: Am J Respir Crit Care Med.

Kim, T., Kim, J., Tae, Y., Park, C., Choi, J.-H., and Choo, J. Reversible instance normalization for accurate time-series forecasting against distribution shift. In *International Conference on Learning Representations*, 2021.

Kingma, D. P. Adam: A method for stochastic optimization. *arXiv preprint arXiv:1412.6980*, 2014.

Kobler, R., Hirayama, J.-i., Zhao, Q., and Kawanabe, M. Spd domain-specific batch normalization to crack interpretable unsupervised domain adaptation in EEG. In Koyejo, S., Mohamed, S., Agarwal, A., Belgrave, D., Cho, K., and Oh, A. (eds.), *Advances in Neural Information Processing Systems*, volume 35, pp. 6219–6235. Curran Associates, Inc., 2022.

Marcus, C. L., Moore, R. H., Rosen, C. L., Giordani, B., Garetz, S. L., Taylor, H. G., Mitchell, R. B., Amin, R., Katz, E. S., Arens, R., Paruthi, S., Muzumdar, H., Gozal, D., Thomas, N. H., Ware, J., Beebe, D., Snyder, K., Elden, L., Sprecher, R. C., Willging, P., Jones, D., Bent, J. P., Hoban, T., Chervin, R. D., Ellenberg, S. S., Redline, S., and Childhood Adenotonsillectomy Trial (CHAT). A randomized trial of adenotonsillectomy for childhood sleep apnea. *The New England Journal of Medicine*, 368(25):2366–2376, June 2013. ISSN 1533-4406. doi: 10.1056/NEJMoa1215881.

O'Reilly, C., Gosselin, N., and Carrier, J. Montreal archive of sleep studies: an open-access resource for instrument benchmarking and exploratory research. *Journal of sleep research*, 23, 06 2014. doi: 10.1111/jsr.12169.

Paszke, A., Gross, S., Massa, F., Lerer, A., Bradbury, J., Chanan, G., Killeen, T., Lin, Z., Gimelshein, N., Antiga, L., Desmaison, A., Kopf, A., Yang, E., DeVito, Z., Raison, M., Tejani, A., Chilamkurthy, S., Steiner, B., Fang, L., Bai, J., and Chintala, S. Pytorch: An imperative style, high-performance deep learning library. In *Advances in Neural Information Processing Systems (NeurIPS)*, pp. 8024–8035. Curran Associates, Inc., 2019.

Pedregosa, F., Varoquaux, G., Gramfort, A., Michel, V., Thirion, B., Grisel, O., Blondel, M., Prettenhofer, P., Weiss, R., Dubourg, V., Vanderplas, J., Passos, A., Cournapeau, D., Brucher, M., Perrot, M., and Duchesnay, E. Scikit-learn: Machine Learning in Python. *Journal of Machine Learning Research*, 12:2825–2830, 2011.

Perslev, M., Jensen, M., Darkner, S., Jenum, P. J., and Igel, C. U-time: A fully convolutional network for time series segmentation applied to sleep staging. *Advances in Neural Information Processing Systems*, 32, 2019.

Perslev, M., Darkner, S., Kempfner, L., Nikolic, M., Jenum, P., and Igel, C. U-Sleep: resilient high-frequency sleep staging. *npj Digital Medicine*, 4:72, 04 2021. doi: 10.1038/s41746-021-00440-5.

Phan, H., Andreotti, F., Cooray, N., Chén, O. Y., and Vos, M. D. SeqSleepNet: End-to-End Hierarchical Recurrent Neural Network for Sequence-to-Sequence Automatic Sleep Staging, February 2019. URL <http://arxiv.org/abs/1809.10932>. arXiv:1809.10932.

Phan, H., Chen, O. Y., Tran, M. C., Koch, P., Mertins, A., and Vos, M. D. XSleepNet: Multi-view sequential model for automatic sleep staging. *IEEE Transactions on Pattern Analysis and Machine Intelligence*, 44(09):5903–5915, sep 2022. ISSN 1939-3539. doi: 10.1109/TPAMI.2021.3070057.

Phan, H., Lorenzen, K. P., Heremans, E., Chén, O. Y., Tran, M. C., Koch, P., Mertins, A., Baumert, M., Mikkelsen, K. B., and De Vos, M. L-SqSleepNet: Whole-cycle Long Sequence Modeling for Automatic

Sleep Staging. *IEEE Journal of Biomedical and Health Informatics*, 27(10):4748–4757, October 2023. ISSN 2168-2208. doi: 10.1109/JBHI.2023.3303197. URL <https://ieeexplore.ieee.org/document/10210638/?arnumber=10210638>. Conference Name: IEEE Journal of Biomedical and Health Informatics.

Quan, S., Howard, B., Iber, C., Kiley, J., Nieto, F., O’Connor, G., Rapoport, D., Redline, S., Robbins, J., Samet, J., and Wahl, P. The sleep heart health study: Design, rationale, and methods. *Sleep*, 20:1077–85, 01 1998. doi: 10.1093/sleep/20.12.1077.

Redline, S., Tishler, P. V., Tosteson, T. D., Williamson, J., Kump, K., Browner, I., Ferrette, V., and Krejci, P. The familial aggregation of obstructive sleep apnea. *American Journal of Respiratory and Critical Care Medicine*, 151 (3 Pt 1):682–687, March 1995. ISSN 1073-449X. doi: 10.1164/ajrccm/151.3.Pt_1.682.

Ronneberger, O., Fischer, P., and Brox, T. U-net: Convolutional networks for biomedical image segmentation. In *Medical image computing and computer-assisted intervention–MICCAI 2015: 18th international conference, Munich, Germany, October 5-9, 2015, proceedings, part III 18*, pp. 234–241. Springer, 2015.

Rosen, C. L., Larkin, E. K., Kirchner, H. L., Emancipator, J. L., Bivins, S. F., Surovec, S. A., Martin, R. J., and Redline, S. Prevalence and risk factors for sleep-disordered breathing in 8- to 11-year-old children: association with race and prematurity. *The Journal of Pediatrics*, 142(4):383–389, April 2003. ISSN 0022-3476. doi: 10.1067/mpd.2003.28.

Rosen, C. L., Auckley, D., Benca, R., Foldvary-Schaefer, N., Iber, C., Kapur, V., Rueschman, M., Zee, P., and Redline, S. A multisite randomized trial of portable sleep studies and positive airway pressure autotitration versus laboratory-based polysomnography for the diagnosis and treatment of obstructive sleep apnea: the HomePAP study. *Sleep*, 35(6):757–767, June 2012. ISSN 1550-9109. doi: 10.5665/sleep.1870.

Schirrmeister, R. T., Springenberg, J. T., Fiederer, L. D. J., Glasstetter, M., Eggensperger, K., Tangermann, M., Hutter, F., Burgard, W., and Ball, T. Deep learning with convolutional neural networks for EEG decoding and visualization. *Human Brain Mapping*, 38(11):5391–5420, November 2017. ISSN 1065-9471, 1097-0193. doi: 10.1002/hbm.23730. URL <http://arxiv.org/abs/1703.05051>. arXiv:1703.05051 [cs].

Spira, A. P., Blackwell, T., Stone, K. L., Redline, S., Cauley, J. A., Ancoli-Israel, S., and Yaffe, K. Sleep-disordered breathing and cognition in older women. *Journal of the American Geriatrics Society*, 56(1):45–50, January 2008. ISSN 1532-5415. doi: 10.1111/j.1532-5415.2007.01506.x.

Stephansen, J. B., Olesen, A. N., Olsen, M., Ambati, A., Leary, E. B., Moore, H. E., Carrillo, O., Lin, L., Han, F., Yan, H., Sun, Y. L., Dauvilliers, Y., Scholz, S., Barateau, L., Hogl, B., Stefani, A., Hong, S. C., Kim, T. W., Pizza, F., Plazzi, G., Vandi, S., Antelmi, E., Perrin, D., Kuna, S. T., Schweitzer, P. K., Kushida, C., Peppard, P. E., Sorensen, H. B. D., Jennum, P., and Mignot, E. Neural network analysis of sleep stages enables efficient diagnosis of narcolepsy. *Nature Communications*, 9(1), dec 2018. doi: 10.1038/s41467-018-07229-3.

Sun, B. and Saenko, K. Deep CORAL: Correlation Alignment for Deep Domain Adaptation, July 2016. URL <http://arxiv.org/abs/1607.01719>. arXiv:1607.01719 [cs].

Ulyanov, D. Instance normalization: The missing ingredient for fast stylization. *arXiv preprint arXiv:1607.08022*, 2016.

Virtanen, P., Gommers, R., Oliphant, T., Haberland, M., Reddy, T., Cournapeau, D., Burovski, E., Peterson, P., Weckesser, W., Bright, J., van der Walt, S., Brett, M., Wilson, J., Millman, J., Mayorov, N., Nelson, A., Jones, E., Kern, R., Larson, E., Carey, C., Polat, I., Feng, Y., Moore, E., VanderPlas, J., Laxalde, D., Perktold, J., Cimrman, R., Henriksen, I., Quintero, E., Harris, C., Archibald, A., Ribeiro, A., Pedregosa, F., van Mulbregt, P., and SciPy 1.0 Contributors. SciPy 1.0: Fundamental Algorithms for Scientific Computing in Python. *Nature Methods*, 17: 261–272, 2020.

Welch, P. The use of fast fourier transform for the estimation of power spectra: a method based on time averaging over short, modified periodograms. *IEEE Transactions on audio and electroacoustics*, 15(2):70–73, 1967.

Zhang, G.-Q., Cui, L., Mueller, R., Tao, S., Kim, M., Rueschman, M., Mariani, S., Mobley, D., and Redline, S. The National Sleep Research Resource: towards a sleep data commons. *Journal of the American Medical Informatics Association: JAMIA*, 25(10):1351–1358, October 2018. ISSN 1527-974X. doi: 10.1093/jamia/ocx064.

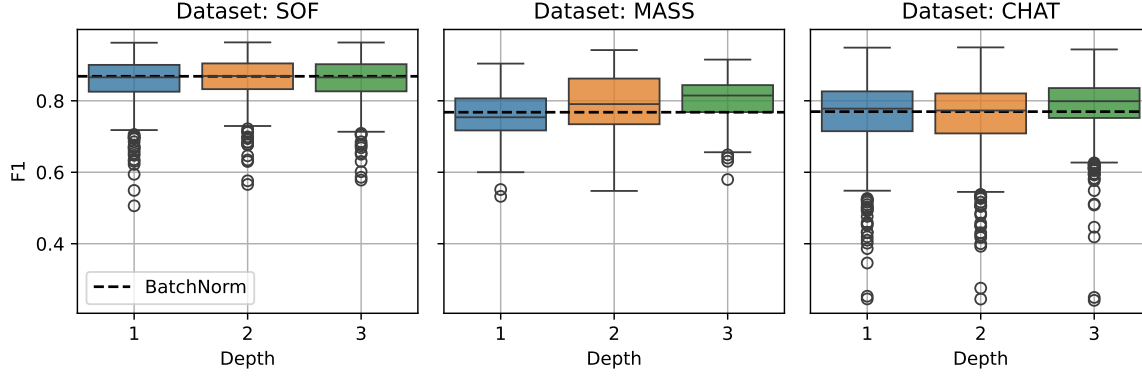


Figure 5: Impact of the depth of application of PSDNorm on the Test datasets F1 score. The black dotted line represents the median of the BatchNorm F1 score.

A. Appendix

A.1. Sensitivity analysis of the depth for PSDNorm

In this section, we investigate the impact of the depth of application of PSDNorm on the performance of the model. The USleep is composed of 12 encoders and 12 decoders, each with a convolutional layer followed by a non-linearity. We chose to compensate the shift at the beginning of the network to avoid propagating the shift through the network. We apply PSDNorm at different depths of the network, from the first encoder to the first three encoders. The filter size is set to 16 for the first encoder and halved for each subsequent encoder. The results are presented in Figure 5.

When we apply PSDNorm only on the first encoder, we see that the performances struggle to improve compare to the BatchNorm (*i.e.*, the black dotted line). However, when we apply PSDNorm on the first two encoders, the performances improve slightly especially for MASS dataset. Finally, when we apply PSDNorm on the first three encoders, the performances improve significantly for all datasets, with a big improvement for MASS and CHAT datasets.

This experiment shows that using the benefit of the depth of neural network to compensate the shift along the network is crucial to improve the performances of the model. This highlights the importance of the PSDNorm to compensate the shift at each layer of the network.

A.2. Proof of the Bures-Wasserstein geodesic (11) between covariance matrices of structure (5)

Proposition A.1. *Let $\Sigma^{(s)}$ and $\Sigma^{(t)}$ be two covariance matrices in $\mathbb{R}^{cf \times cf}$ following (5). Let us denote $\mathbf{P}^{(s)}$ and $\mathbf{P}^{(t)}$ the corresponding PSD matrices. The geodesic associated with the Bures-Wasserstein metric between $\Sigma^{(s)}$ and $\Sigma^{(t)}$ and parameterized by $\alpha \in [0, 1]$ is $\Sigma(\alpha)$ following (5) of PSD*

$$\mathbf{P}(\alpha) = \left((1 - \alpha) \mathbf{P}^{(s) \odot \frac{1}{2}} + \alpha \mathbf{P}^{(t) \odot \frac{1}{2}} \right)^{\odot 2}.$$

Proof. From (Bhatia et al., 2019), the geodesic associated with the Bures-Wasserstein metric between two covariance matrices $\Sigma^{(s)}$ and $\Sigma^{(t)}$ is given by

$$\gamma(\alpha) = (1 - \alpha)^2 \Sigma^{(s)} + \alpha^2 \Sigma^{(t)} + \alpha(1 - \alpha) \left[(\Sigma^{(s)} \Sigma^{(t)})^{\frac{1}{2}} + (\Sigma^{(t)} \Sigma^{(s)})^{\frac{1}{2}} \right]. \quad (14)$$

where

$$(\Sigma^{(s)} \Sigma^{(t)})^{\frac{1}{2}} = \Sigma^{(s) \frac{1}{2}} \left(\Sigma^{(s) \frac{1}{2}} \Sigma^{(t)} \Sigma^{(s) \frac{1}{2}} \right)^{\frac{1}{2}} \Sigma^{(s) - \frac{1}{2}}. \quad (15)$$

Since $\Sigma^{(s)}$ and $\Sigma^{(t)}$ diagonalize in the unitary basis $\mathbf{I}_c \otimes \mathbf{F}_f$, $\gamma(\alpha)$ also diagonalizes in this basis. Thus, we only have to compute the geodesic between the PSD matrices $\mathbf{P}^{(s)}$ and $\mathbf{P}^{(t)}$ and from now on, all operations are element-wise. Let $\mathbf{P}(\alpha)$

be the PSD of $\gamma(\alpha)$, we have

$$\mathbf{P}(\alpha) = (1 - \alpha)^2 \mathbf{P}^{(s)} + \alpha^2 \mathbf{P}^{(t)} + \alpha(1 - \alpha) \left[(\mathbf{P}^{(s)} \odot \mathbf{P}^{(t)})^{\odot \frac{1}{2}} + (\mathbf{P}^{(t)} \odot \mathbf{P}^{(s)})^{\odot \frac{1}{2}} \right] \quad (16)$$

$$= (1 - \alpha)^2 \mathbf{P}^{(s)} + \alpha^2 \mathbf{P}^{(t)} + 2\alpha(1 - \alpha) (\mathbf{P}^{(s)} \odot \mathbf{P}^{(t)})^{\odot \frac{1}{2}} \quad (17)$$

$$= \left((1 - \alpha) \mathbf{P}^{(s) \odot \frac{1}{2}} + \alpha \mathbf{P}^{(t) \odot \frac{1}{2}} \right)^{\odot 2}. \quad (18)$$

This concludes the proof. ■